ADVANCED ELECTRONIC MATERIALS
www.advelectronicmat.de

Theoretical and Experimental Investigations on the Aggregation-Enhanced Emission from Dark State: Vibronic Coupling Effect

Ping-An Yin, Qing Wan, Yingli Niu, Qian Peng, Zhiming Wang,* Yuxuan Li, Anjun Qin, Zhigang Shuai,* and Ben Zhong Tang**

Aggregation-induced/-enhanced emission (AIE/AEE) has aroused broad interest. The mechanism behind is understood as the aggregation restriction of the nonradiative decay from electronically excited state to the ground state, either through interconversion or through conical intersection, leaving the dipole-allowed radiative decay channel relatively intact. Here, a report on an AEE phenomenon for 5,10-diphenylphenazine (DPhPZ) compound is presented, for which the experiment shows to be AEE active but the lowest excited state has been long known to be "dark state," namely with zero transition dipole with the ground state according to Kasha's rule. The computational studies demonstrate that the optical emission stems from the "dark state" with emission intensity borrowed from higher-lying "bright state" through Herzberg–Teller vibronic coupling, and the resultant spectra are in good agreement with the experiment in terms of both line shape and peak position. The vibronic-coupling-induced radiative decay and the restricted nonradiative decay synergistically bring about highly efficient luminescence of DPhPZ in the solid phase. The findings open a new avenue for the development of solid-emissive luminophores.

1. Introduction

Organic solid-state luminescence has recently attracted rapidly increasing interest for its promising applications in solid-state lighting, flat panel display, optical communication, and so on.[1,2] In contrast to the traditional aggregation-caused quenching in the solid phase, Tang and co-workers introduced the concept of aggregation-induced emission (AIE) in 2001.[3] Since then, a great number of scientists have followed this direction of research and great advancements have been achieved, in the synthesis of a variety of AIEgens,[4–10] in the understanding of AIE mechanisms,[11–13] in revealing the AIE dependence on the morphological structures,[14–17] and in the exploration of novel technological applications.[18–24]

Many efforts have been devoted to reveal the inherent mechanism through a myriad of experimental and theoretical means. Earlier work by Oelkrug et al. has demonstrated the role of J-aggregation for the enhanced solid-state emission.[25] The restriction of the intramolecular rotation was proposed first through the temperature-, viscosity-, and intramolecular-steric-hindrance-dependent luminescence quantum efficiency experimentally measured. Then, the restriction of the intramolecular vibration,[21] and restriction of intermolecular motion,[11] was widely found to be responsive for the strong luminescence in solid phase combining experimental measurements and theoretical calculations. In theory, the block

P.-A. Yin, Dr. Q. Wan, Prof. Z. Wang, Y. Li, Prof. A. Qin, Prof. B. Z. Tang,
Center for Aggregation-Induced Emission
Key Laboratory of Luminescence from Molecular Aggregates of Guangdong Province
SCUT–HKUST Joint Research Institute
State Key Laboratory of Luminescent Materials and Device
South China University of Technology
No. 381 Wushan Road, Tianhe District, Guangzhou 510640, P. R. China
E-mail: wangzhiming@scut.edu.cn; tangbenz@ust.hk

P.-A. Yin, Prof. Q. Peng
Key Laboratory of Organic Solids
Beijing National Laboratory for Molecular Sciences (BNLMS)
Institute of Chemistry, Chinese Academy of Sciences
Beijing 100080, P. R. China
E-mail: qpeng@iccas.ac.cn

The ORCID identification number(s) for the author(s) of this article can be found under https://doi.org/10.1002/aelm.202000255.

DOI: 10.1002/aelm.202000255

Dr. Y. Niu
Department of Physics
School of Science
Beijing Jiaotong University
Beijing 100044, P. R. China

Prof. Z. Shuai
Department of Chemistry and MOE Key Laboratory of Organic Optoelectonics and Molecular Engineering
Tsinghua University
Beijing 100084, P. R. China
E-mail: zgshuai@tsinghua.edu.cn

Prof. B. Z. Tang
Department of Chemistry
Hong Kong Branch of Chinese National Engineering Research Center for Tissue Restoration and Reconstruction
and Institute for Advanced Study
The Hong Kong University of Science and Technology
Clear Water Bay, Kowloon, Hong Kong, China

of the nonradiative decay channels in rigid environment makes the radiative dominate to recover the strong fluorescence, which has been widely proved by many experimental means, such as resonance Raman spectrum, isotope effect, the nanoparticle size-dependence relationship of fluorescence intensity, and so on.[26–29] Later on, a number of additional scenario have been suggested, including the aggregation-restricted access to conical interaction,[30,31] the blockage of access to dark state via isomerization,[32] the restriction of E/Z isomerization process,[33] the excited-state intramolecular proton transfer,[34] etc. In fact, most of the proposed mechanisms are based on the aggregation restriction to the various nonradiative processes. The prerequisite is that the radiative decay channel is strongly electric dipole-transition allowed ("bright state") and relatively intact in both solution and aggregate phase. However, if the lowest-lying excited state is symmetry forbidden,[35] or very weakly allowed for the donor–acceptor systems with charge transfer character[36] and/or with different orbital types[37] (e.g., n–π^* orbitals or σ–π^* orbitals) and so on, the fluorescence radiative decay is vanishingly small with the evanescent oscillator strength. According to Einstein's spontaneous emission theory, the radiative decay rate is expressed as:

$$k_r = \frac{8\pi^2 \nu_{fi}^3}{3\varepsilon_0 \hbar c^3} \mu_{fi}^2 \approx \frac{f\nu_{fi}^2}{1.5}$$ where μ_{fi} is the transition electric dipole between the excited state and the ground state, f is the dimensionless oscillator strength, and if the transition energy ν_{fi} is expressed in wavenumber, the dimension of k_r is in the unit of s^{-1}. So, if the transition dipole is zero, the radiaive decay vanishes.

The interaction between electronic and nuclear motion, alias vibronic coupling can "borrow" intensities from other intermediate allowed states through certain normal modes,[38] namely, the Herzberg–Teller (HT) effect.[39] It has been found in the absorption, emission, Raman, and circular dichroism spectra[40–42] in porphyrin and its derivatives,[43] dioxaborine heterocycles,[44] benzene derivatives, and C_{60} in the gas phase or in solution.[45,46] However, the HT effect in the solid-state luminescence has been rarely considered and the influence of aggregation on the vibronic transition has been scarcely investigated.[47]

In this work, we carry out systematic investigations on an aggregation-enhanced emission (AEE) behavior from the dipole-forbidden excited state for 5,10-diphenylphenazine (DPhPZ) compound through experiments and theoretical calculations. Using the quantum mechanics (QM)/ molecular mechanics (MM) method and the thermal vibration correlation function rate theory, we figure out that the optical emission stems from the dark state with emission intensity borrowed from higher bright state through vibronic coupling. Combined the vibronic-coupling-induced radiative and the restricted nonradiative decay from solution to the solid phase, the AEE mechanism is well illustrated for the dark-state system. To the best of our knowledge, it is reported for the first time that the AEE can happen on the dark state, and its mechanism is revealed in detail through comprehensive theoretical and experimental investigations.

2. Experimental Synthesis and Characterizations

5,10-dihydrophenazine (DHPZ) is a classical fluorochrome group, which is usually used to construct the molecules with anomalous photophysics, such as multiple emissions and thermally activated delayed fluorescence.[48,49] Its derivative, DPhPZ compound is also expected to exhibit unusual photophysical behaviors. The synthesis, purification, NMR characterization, as well as various spectroscopies of DPhPZ have been carefully carried out, as shown in the Supporting Information. Molecular structure, experimentally determined crystal structure, optical spectroscopy for solution, film, and crystals, as well as the aggregation-enhanced optical density ratio in tetrahydrofuran (THF)/water mixture are shown in **Figure 1**. From the crystal structure in Figure 1a, it is seen that i) the packing is not compact and the π–π interaction is not effective; ii) but the hydrogen bonds are strong as shown by the distances. It is seen that the shortest intermolecular C—H distance is 2.752 Å. Thus, intermolecular electrostatic interactions are expected to play some role for the optical property.

The fluorescent spectra showed close maximum peaks of 463, 469, and 470 nm, respectively, for the DPhPZ in the solution, thin film, and crystalline phase with similar line shape (Figure 1b). These indicate that the emissions stem from the same electronic excited state. The spectra also manifest profound vibrational resolved structure, implying molecular rigidity in all the three phases. Interestingly, the relative intensity of shoulder peaks around 541 nm for crystal undergoes large enhancement from solution. This indicates that intermolecular interaction can alter the vibronic coupling.

We carefully examined the fluorescence lifetimes of all emission peaks in solution, film, and solid states (Figure S5, Supporting Information). In the THF solution, three emission peaks showed similar lifetime (7.67, 8.05, 8.11 ns), and the lifetime from aggregation state (46.3, 46.1, 42.4.ns) was longer than that in THF solution. And, all the emission peaks had similar lifetime, suggesting the same excited-state species. **Table 1** presents the measured photophysical data for the compounds in all the three phases. The quantum luminescence efficiency increases from 3.5% in THF solution, to 9.4% in thin film, then to 11.3% in crystal, showing typical aggregation-enhanced emission characteristics. The typical AEE curve was obtained upon addition of poor solvent water into THF solutions: the emission peak height versus water content (%) is shown in Figure 1c.

3. Theoretical Results and Discussion

3.1. Molecular Geometry and Excited State Structure

To gain theoretical understanding of the AEE in DPhPZ, we first employ the quantum chemistry calculations with polarizable continuum model (PCM) considering for solvent effect, and ONIOM model containing 72 molecules from the single crystal structure to mimic the solid-state environment, see **Figure 2**a. The geometrical and electronic structures and vibrational modes of the S_0 and S_1 states were optimized and calculated at (TD)M062X/CC-PVDZ level. Then, these quantum chemical data are used as input for the following photophysical property evaluation using the molecular material property prediction package program developed by Shuai and co-workers.[50–53] The rectangular coordinate is defined in Figure 2b. Phenazine (PZ) core bents along the N1–N2 axis (γ) and the intersecting planes of the two aryl rings along the N1–N2 axis form a bay with the bent angle α between

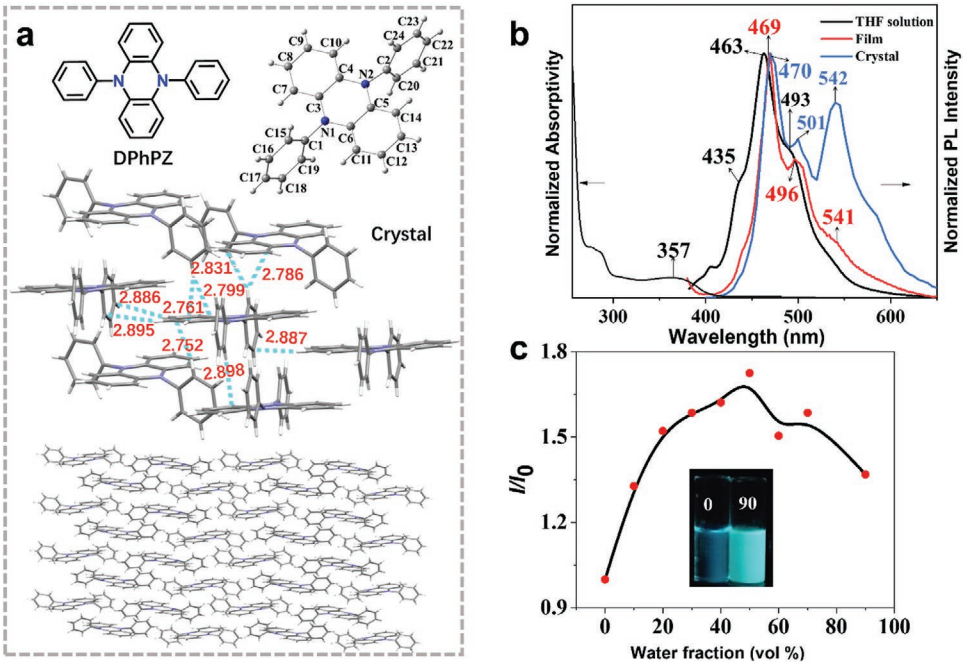

Figure 1. a) The molecular structure, packing structure in crystal. b) The absorption in THF (black, thin), and emission spectra in THF (black), film (red), and crystal phases (blue) at λ_{ex} = 362 nm. c) The plot of emission intensity ratio I/I_0 versus water fraction, where I_0 is the photoluminescence (PL) intensity in pure THF.

planes P1 and P2. The θ_1 and θ_2 are the supplement angle of the ∠C1N1N2 and ∠C2N2N1, respectively. The β_1 and β_2 characters the twisting degree of the phenyl rings P3 and P4 relative to plane σ_{xy}, respectively. Thus, there are two symmetry axes C_2 (y- and z-axes) and two symmetry planes (σ_{yz} and σ_{xz}) in DPhPZ and it belongs to C_{2v} point group when $\theta_1 = \theta_2$. Otherwise, its symmetry would break down to C_1 point group when $\theta_1 \neq \theta_2$.

The optimized geometries with main parameters are presented in **Figure 3**a and Tables S5 and S6 (Supporting Information) for the S_0 and S_1 states of DPhPZ in solution and the solid phases, as well as the crystal structure for comparison. The calculated S_0-geom of DPhPZ in cluster (e.g., $\alpha = 176.59°$, $\theta_1 = 6.70°$, and $\theta_2 = 20.40°$) is in good agreement with the available experimental crystal structure ($\alpha = 174.75°$, $\theta_1 = 3.12°$, and $\theta_2 = 17.82°$). By symmetry analysis, the S_0-geom belongs to C_{2v} point group in solution, and the C_{2v} symmetry is maintained, but the dihedral angle α increases from 164.48° to 180.00° and θ is reduced to zero for the S_1-geom, which is consistent with the photoinduced structural planarization phenomenon.[54] By contrast, the symmetry of DPhPZ is broken to be C_1 point group in the solid phase, although the PZ core keeps the symmetry of C_{2v} in both S_0 and S_1 states. Moreover, from the S_0 to S_1 states in the solid phase, the geometrical structure modification is much less pronounced due to the rigid environment. In addition, there are similar large bond length modifications of C—C and C—N bonds of PZ core and two phenyl rings from the S_0 to S_1 state in the two phases, which would largely affect the photophysical properties.

For the electronic structure in Figure 3b, it is noted that the highest occupied molecular orbital is of A_1 symmetry and is mostly localized on the PZ moiety with electron-donating ability because the phenyl rings (P3 and P4) are perpendicular to PZ moiety. And, the excitation-involved lowest unoccupied molecular orbital (LUMO) (88%) and LUMO+4 (11%) are all of A_2 symmetry, spreading over the whole molecule. Thus, S_1 state is dipole-forbidden by disobeying the symmetry selection rule. In the solid phase, the orbital character and transition property are both similar to those in solution (all the electronic structure analyses of S_0 are shown in Figure S6 in the Supporting Information). Differently, compared with the S_1-geom in solution, the planarity and the perpendicularity are slightly broken owing to the intermolecular interaction, which increases the conjugation between phenyl ring and PZ moiety and strengthens the contribution from phenyl rings to the S_1 state (Figure 2b). As a result, the transition becomes weakly dipole-allowed.

Table 1. The experimentally measured photophysical parameters for DPhPZ.

DPhPZ[a)]	Absorption $S_0 \rightarrow S_1$ λexp [nm](ε [M^{-1} cm^{-1}])	Emission $S_1 \rightarrow S_0$ λexp[nm]	Φ_f[%]	τ_f[ns]	k_r[$\times 10^6$ s^{-1}]	k_{nr}[$\times 10^7$ s^{-1}]
Solution	357	463[b)]	3.5	9.03	3.88	10.70
Film	476	469[b)], 496	9.4	32.76	2.87	2.77
Crystal	–	470[b)], 501, 542	11.3	46.30	2.44	1.92

[a)]The experimental values are taken from the peak wavelength of the absorption and emission; [b)]The wavelength with underline is the maximum peak.

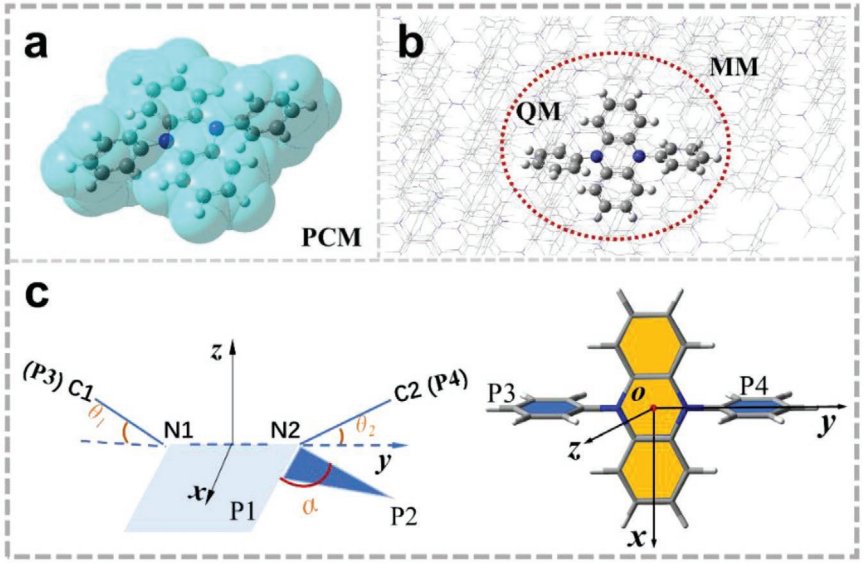

Figure 2. Computational a) PCM and b) ONIOM models. c) The coordinate system with main symmetry axes: α is the dihedral angle between planes P1 and P2; $\theta_1 = 180° - \angle C1N1N2$, $\theta_2 = 180° - \angle C1N2C1$; and β_1/β_2 is the dihedral angle between planes σxy and phenyl ring P3/P4.

3.2. Vibronic Coupling and Herzberg–Teller Effect

Generally, the optical transitions for absorption or fluorescence are discussed theoretically in the frame of Franck–Condon (FC) principle, in which the electronic and nuclear wave functions are decoupled completely, as seen in **Figure 4**a. For the FC transition, the calculated transition dipole moment and oscillator strength (f) for the first excited state S_1 is zero for DPhPZ in solution. In the solid phase, the calculated μ and f of the S_1 state are 0.0880 Debye and 0.0001 for absorption, and 0.0359 Debye and 1.36×10^{-5} for emission (see more details in Tables S1–S4 in the Supporting Information). Note that the experiment indicates weak emission in solution and strong fluorescence in the solid phase. We then consider the HT effect through which the vibronic coupling (interaction between electronic and nuclear vibrational wave functions) can induce optical transition originally forbidden or weakly allowed, as seen in Figure 4a. Namely, the transition dipole μ_{fi} can be expanded at the equilibrium geometry as

$$\vec{\mu}_{fi} = \vec{\mu}_0 + \sum_k \vec{\mu}_k Q_k + \sum_{k,l} \vec{\mu}_{kl} Q_k Q_l + \cdots \quad (1)$$

In the first-order term, the first derivatives of transition dipole moment with respect to the normal mode coordinates can be calculated directly by the numerical method as

$$\vec{\mu}_k \approx \Delta\vec{\mu}_k / \Delta Q_k \quad (2)$$

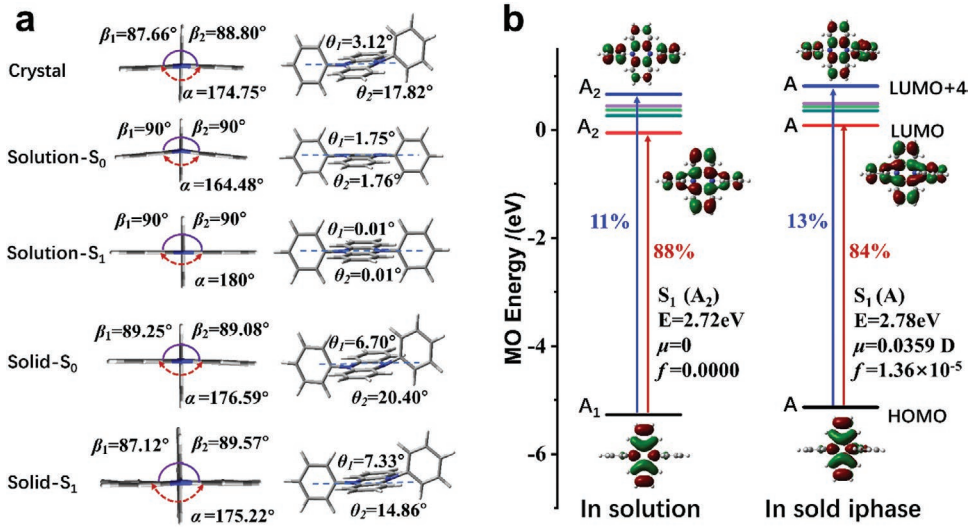

Figure 3. a) The optimized geometries of the S_0 and S_1 states in solution and the solid phase. b) The frontier orbitals and transition properties, including transition components, excitation energy, transition dipole moment, and oscillator strength in solution and the solid phase.

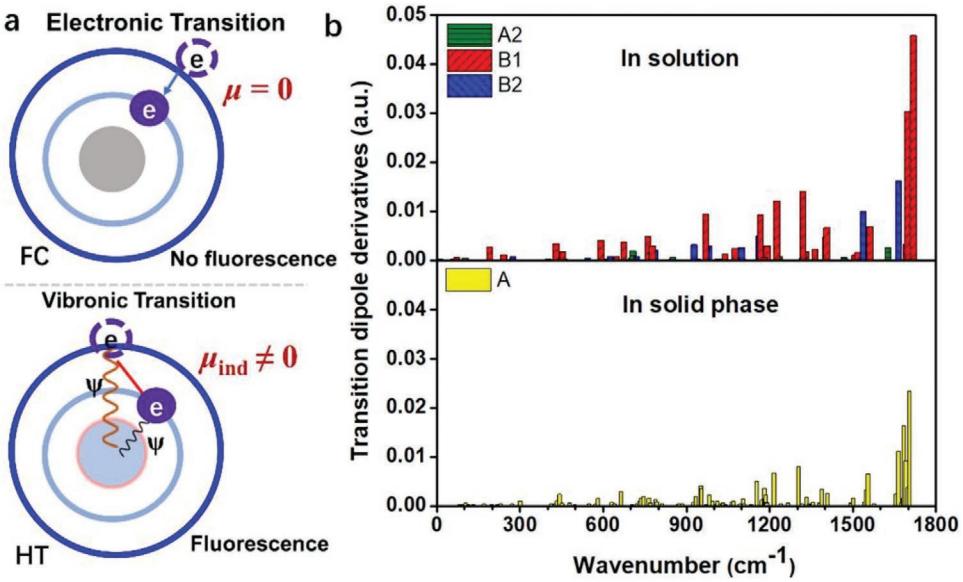

Figure 4. a) The FC and HT physical model. b) The calculated derivatives of transition dipole moment with respect to the normal mode coordinates $\vec{\mu}_k \approx \Delta\vec{\mu}_{fi} / \Delta Q_k$ of DPhPZ in solution and the solid phase.

It can be also expressed as an integration over transition density derivative

$$\vec{\mu}_k = \left(\partial\vec{\mu}_k / \partial Q_k\right)_0 = -e\int d^3x \left(\partial\rho_{fi} / \partial Q_k\right)_0 \vec{r} \equiv -e\int d^3x \rho_k' \vec{r} \quad (3)$$

(The detailed formulas are derived in the Supporting Information) The obtained $\vec{\mu}_k$ are depicted in Figure 4b. In solution, the $\vec{\mu}_k$ with A_2 symmetry mode are polarized along the *z*-axis, $\vec{\mu}_k$ with B_1 symmetry are polarized along the *y*-axis, $\vec{\mu}_k$ with B_2 symmetry are polarized along the *x*-axis, and $\vec{\mu}_k$ with symmetry A_1 are zero, which are consistent with the result referred from selection rule for $\phi_i |(\partial\vec{\mu}_{fi} / \partial Q_k)_0 | \phi_f$. Herein, the normal modes with B_2 and B_1 symmetry make remarkable contributions to $\vec{\mu}_k$. But in the solid phase, the symmetry of DPhPZ reduced to C_1 point group and all the normal modes are of symmetry A. The transition electric dipole becomes weakly allowed and $|\vec{\mu}_k|$ are polarized along all three directions. From the absolute value of $|\vec{\mu}_k|$ in Figure 4b, it can be seen that i) their values are of the same order of magnitude in both phases, indicating similar HT vibronic coupling; ii) the normal modes with 1500–1720 cm^{-1} contribute largely to the $|\vec{\mu}_k|$ in both phases; iii) although the $|\vec{\mu}_k|$ value in general decreases from solution to cluster, there appear more vibrational modes in cluster due to symmetry broken, especially the high-frequency normal modes with ≈1600–1720 cm^{-1}. The total numbers of the vibrational modes for DPhPZ (44 atoms) are 126. From the selected normal modes with spatial distributions of the HT transition dipole $\rho_k'(r)$ with large $|\vec{\mu}_k|$ values in Figure S7 (Supporting Information), it is obvious that in solution, the important normal modes span a wide range from 1200 to 1700 cm^{-1}, including normal modes 1299.52, 1664.63, 1676.25, and 1696.72 cm^{-1}. While in cluster, they concentrate on the high-frequency normal modes at 1600–1720 cm^{-1}, including normal modes 1664.98, 1675.33, 1683.75, and 1703.70 cm^{-1}. The increasing contribution from high-frequency normal modes would have an important effect on the line shape of the fluorescence spectrum. From the displacement vectors, we can know that mode 1299.52 cm^{-1} is assigned as the stretching vibration of six C—N bonds; the others are the stretching vibrations of C=C bonds of the molecules, especially C=C bonds in PZ core. Overall, when DPhPZ going to the solid phase from solution, owing to the breaking of symmetry, more stretching vibrations of C=C bonds join in the vibronic transitions and increase the intensity of the vibration satellites in the long wavelength region of the emission spectrum.

3.3. Optical Spectra and Origin of AEE

Considering HT effect, the simulated absorption spectrum of the $S_0 \rightarrow S_1$ in Figure S8 (Supporting Information) successfully reproduces the long wavelength band at 300–400 cm^{-1} of the experimental spectrum for DPhPZ solution in Figure 1b. The experimental and simulated fluorescence spectra are plotted in **Figure 5** for DPhPZ in solution and in the solid phase at 77 and 298 K. It is exciting that the simulated spectra well agree with the experimental ones, including the positions of spectral peaks, line shape with shoulder structures, and the spectral shifts at different temperatures for DPhPZ in both phases. These indicate that HT vibronic couplings dominate the behaviors of absorption and emission spectra for DPhPZ in both phases. At the same time, the current quantum chemistry approach and the thermal vibration correlation function method are reliable and practical. In solution, the fluorescence spectrum has three notable peaks with the calculated values of 428, 459, and 486 nm and the corresponding experimental values of 435, 463, and 493 nm. When lowering temperature, the emission spectrum exhibits more satellite peaks as expected but with noticeable redshifts. Differently, the emission spectrum in the solid phase exhibits more pronounced peaks and

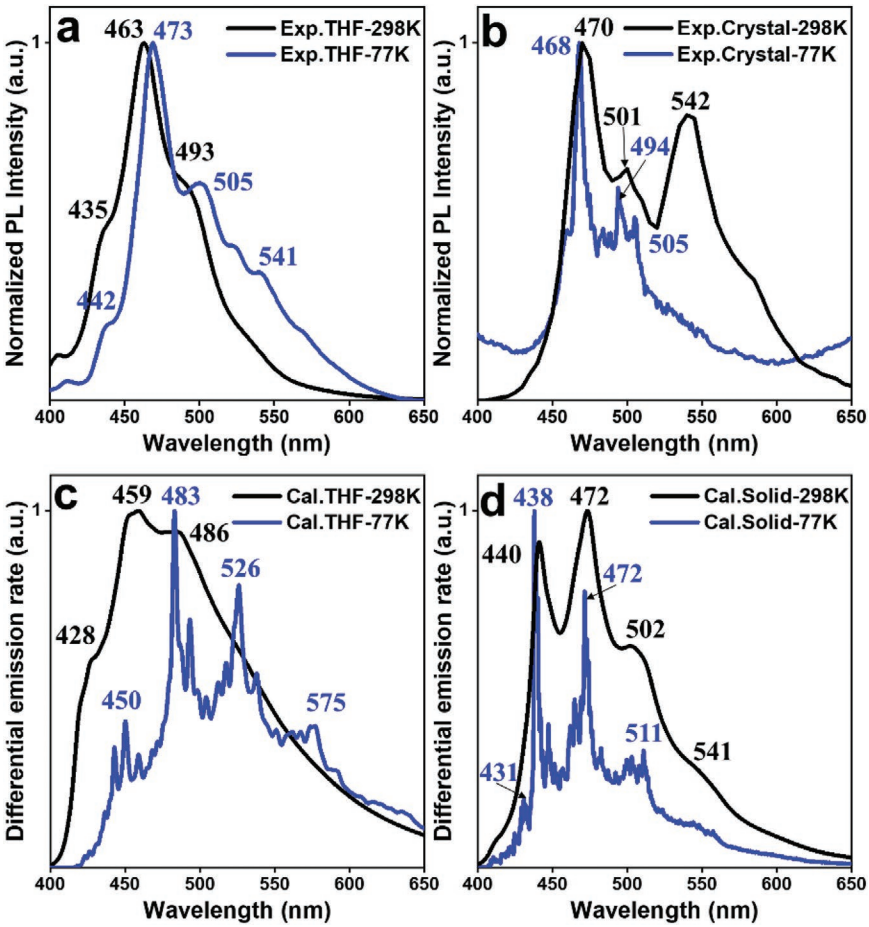

Figure 5. The experimental emission spectra of DPhPZ at 298 and 77 K in a) THF solution, b) crystal; the calculated emission spectra of DPhPZ at 298 and 77 K in c) THF solution, d) solid phase.

hardly demonstrated any dependence on the temperature or position shifts from 298 to 77 K.

In order to understand the spectroscopic behaviors, we further analyze the origin of the spectra. In principle, the total FCHT spectrum is determined by the product of HT vibronic coupling and the FC factor according to the equations in the Supporting Information. The HT vibronic couplings are similar except for a higher-frequency normal mode of 1683.75 cm^{-1} replacing a lower-frequency normal mode of 1299.52 cm^{-1} from solution to solid phase. However, the Frank–Condon factors (Figure S9, Supporting Information) display different natures owing to Huang–Rhys factors changing greatly from solution to solid phase (Figure S10, Supporting Information). In solution, the Huang–Rhys factors are large, and that of a low-frequency mode 41.12 cm^{-1} is larger than 2.0, indicating that they would generate the transitions to higher vibrational states in the emission process.[55] When going to the solid phase, the Huang–Rhys factors become small and the maximum value is smaller than 1.0, suggesting that the 0–0 transition is dominant in the emission process.[55] These suggest that the temperature effect is more obvious in solution than that in the solid phase. The identification of the spectral peaks is given in **Figure 6**. The main emission peaks in solution stem from the combined contribution of HT effect of modes 1664.63, 1676.25, and 1696.72 cm^{-1}, and the 0–1 transition of low-frequency mode 17.43 cm^{-1} and 0–2 transition of mode 41.12 cm^{-1} in FC factor at room temperature. The FC transition properties are almost unchanged, while the contributed HT modes become the highest frequency 3214.37, 3213.81, as well as 869.97 cm^{-1}, which leads to the large redshift of the spectrum at low temperature. In the solid phase, the significant peaks mainly come from the normal modes with HT vibronic coupling and temperature independent 0–0 transition, which explain the weak temperature effect in solid phase. Especially, the newborn peak at 502 nm from solution to solid phase is generated through HT vibronic coupling from mode 1983.75 cm^{-1}, which is absent in the HT spectrum owing to the symmetry-forbidden in solution, and the FC contributions from 0–0 transition which is dipole-forbidden in solution.

More importantly, the calculated radiative decay rate constants agree well with the experimental values in both solution and solid phases after considering the HT vibronic coupling effect, which are 2.62×10^6 and 3.88×10^6 s^{-1} in solution, and 1.99×10^6 and 2.44×10^6 s^{-1} in the solid phase, respectively, for DPhPZ at room temperature (Tables 1 and 2). The averaged induced electronic dipole moments are 1.01 D for solution and 0.78 D for solid phase. It can be known that the aggregation has a slight effect on the radiative decay rates because of similar HT vibronic coupling, although the line shape of fluorescence

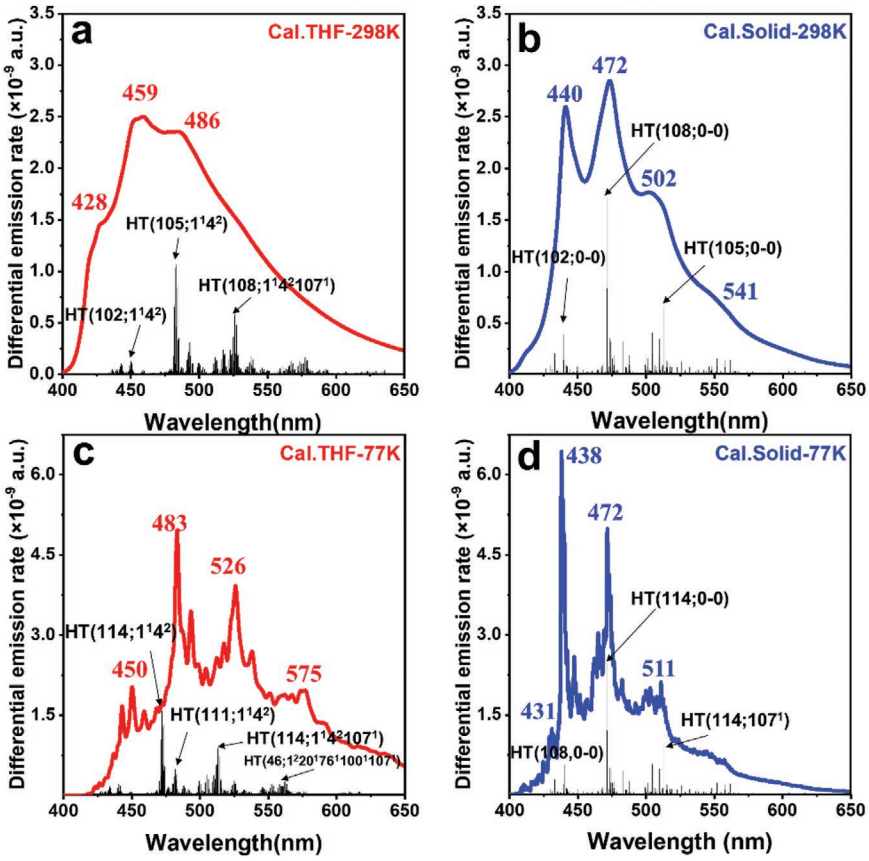

Figure 6. The calculated emission spectra of DPhPZ with HT approximation a,b) at 298K and c,d) at 77K in THF solution and solid phase. In HT(M,N^x), M denotes mode index with HT effect; N is the mode index in FC factor; and x means the transition from 0 to high vibrational state.

spectrum is affected. The nonradiative decay rate is reduced more than two orders of magnitude from solution to solid phases (**Table 2**) owing to the sensibility of the reorganization energy to the rigid environment. The reorganization energy characterizes the electron-vibration couplings in the nonradiative decay process and controls the nonradiative decay rate to large extent.[27,28] It is largely decreased from 3022 to 2550 cm^{-1} (Figure S11, Supporting Information) due to the restriction of molecular geometrical structure relaxation in the solid phase, which results in the significant decrease of the nonradiative rate constant. Thus, the AEE of DPhPZ can be well explained by the coupled-vibronic-transition-induced radiative with suppressed nonradiative decay. However, there exists a discrepancy between the calculated and the experimental nonradiative decay rate constants, and the measured one is only reduced less than one order of magnitude, while the theoretical value is more than two orders of magnitude. In fact, the theoretical model has ignored the intermolecular electronic and excitonic couplings, which could underestimate the nonradiative decay at the aggregate. Nevertheless, the qualitative trend agrees with the experiment, thus can reveal the underlying mechanism behind the aggregation-enhanced emission from dark state.

Table 2. The calculated radiative and nonradiative decay rate constants of DPhPZ with and without HT effect in solution and solid phases at room temperature.

DPhPZ	FC			FCHT	
	k_{nr} [$\times 10^7$ s^{-1}]	k_r [$\times 10^6$ s^{-1}]	Φ_f [%]	k_r [$\times 10^6$ s^{-1}]	Φ_f [%]
Solution	13.20	0.00	0.0	2.62	1.9
Solid	0.0248	0.0247	9.0	1.99	89.0

4. Conclusion

To summarize, we have demonstrated the AEE phenomenon from dark state both theoretically and experimentally. Our experiments show that DPhPZ is a typical AEE-active compound with quantum efficiency increasing from 3.5% in solution to 9.4% in thin film, then to 11.3% in crystal. Quantum chemistry calculations demonstrated that its lowest excited state of DPhPZ is of dipole-forbidden symmetry, i.e., dark state. The optical emission stems from the Herzberg–Teller effect, namely, the intensity borrowing through vibronic coupling. Both the calculated absorption and fluorescence spectra considering the HT term are in good agreement with the experiments in both solution and solid phases. And, compared to the emission spectrum in solution, the new striking peak at 502 nm in the solid phase is generated through HT vibronic coupling from normal mode 1983.75 cm^{-1} and the FC contributions from 0–0 transition. For the first time, we demonstrate

that AEE can happen for emission from dark state. Using the QM/MM calculation in conjunction with the rate formalism based on thermal vibration correlation function we developed earlier, we quantitatively calculated the radiative and nonradiative decay rates, and well rationalized the AEE phenomenon. The intermolecular interactions slightly change the radiative decay, while they greatly strengthen the rigid of the molecule, largely blocking the nonradiative decay channels and greatly slowing down the nonradiative decay for DPhPZ in aggregate. There exist quantitative discrepancies between the calculated nonradiative decay rate, most probably due to the neglects of intermolecular electronic and excitonic couplings, which i) either can give rise to luminescence quenching, reducing radiative decay, or ii) further increase the nonradiative decay rate. Yet, both the calculated line shapes and peak positions for absorption and emission agree with the measurements, and the calculated qualitative trend of excited state decay rates renders reasonable explanation for the AEE phenomenon from dark state. It remains a challenging issue to make prediction for the excited state dynamics at the nano- to microsecond time scale for complex system. Overall, the efficient solid-state emission for dark state is achieved and deeply understood by combining Herzberg–Teller vibronic-coupling-induced radiative and the suppressed nonradiative decay, which provide novel platforms for designing excellent solid-emissive luminophores.

5. Experimental Section

Materials: PZ, sodium dithionite, sodium *tert*-butoxide, and tri-*tert*-butylphosphonium tetrafluoroborate ($HPtBu_3BF_4$) were purchased from Energy Chemical Co. and used without further purification. All solvents were dried prior to use with appropriate drying agents. Column chromatography was performed using silica gel 60 (100–200 mesh).

Synthesis and Characterization: Phenazine (2.5 g, 14 mmol) and sodium dithionite (25 g, 140 mmol) were put into flask. The degassed mixture solvent of ethanol/water (v/v = 80/250) was injected into flask and refluxed under N_2 atmosphere for 4 h. After reaction and cooling to room temperature, the mixture was filtrated and washed with ethanol and water for 3 times. The intermediate product (DHPZ) was obtained as light green powder. The crude DHPZ was directly used for next reaction without further purification. DHPZ (2 g), bromobenzene (3.1 g, 20 mmol), $HPtBu_3BF_4$ (580 mg, 2 mmol), Na^tOBu (5.76 g, 60 mmol), $Pd_2(dba)_3$. $CHCl_3$ (104 mg, 1 mmol) were dried under vacuum for 30 min in a two-neck 250 mL round-bottomed flask fitted with a reflux condenser. The flask was back-filled with N_2 and dry toluene (60 mL) was added. The reaction was then heated to 115 °C with stirring for 24 h. At the end of the reaction, water was added. The mixture was extracted with dichloromethane (DCM) for 3 times. The pure product was received by chromatography using DCM/petroleum as the eluent to afford a red powder (2.7 g).

$^1H/^{13}C$-NMR spectra were recorded on a Bruker 500 (500 MHz) spectrometer in deuterated benzene using tetramethylsilane as internal reference. ^1H NMR (500 MHz, d-dimethyl sulfoxide (DMSO)) δ = 7.71 (t, 4H), 7.55 (t, 2H), 7.43 (d, 4H), 6.27 (m, 4H), 5.50 (m, 4H). ^{13}C NMR (500 MHz, d-DMSO): 139.96, 136.47, 132.08, 131.32, 128.97, 121.33, 112.58. HRMS ($C_{24}H_{18}N_2$): *m/z* 334.1474 [M+, calcd 334.1470].

X-Ray Single Crystal Diffraction Analysis: Single crystal monochromatic X-ray diffraction measurements were carried out on a Bruker D8 Venture diffractometer outfitted with a PHOTON-100 complementary metal–oxide–semiconductor detector, using microfocus Mo Kα radiation (λ = 0.71073 Å) that was operated at 50 kV and 40 mA at 123 K by chilled nitrogen flow controlled by a KRYOFLEX II low temperature attachment.

Optical Measurements: UV–vis absorption spectrum was measured on a Shimadzu UV-2600 spectrophotometer. PL spectra were recorded on a Horiba Fluoromax-4 spectrofluorometer. Fluorescence quantum yields were measured using a Hamamatsu absolute PL quantum yield spectrometer C11347 Quantaurus_QY.

Supporting Information

Supporting Information is available from the Wiley Online Library or from the author.

Acknowledgements

P.-A.Y. and Q.W. contributed equally to this work. This work was supported by the National Natural Science Foundation of China (Grant Nos. 21788102, 21973099, 51673118, and 21975077), the Ministry of Science and Technology of China (Grant No. 2017YFA0204501), the Fundamental Research Funds for the Central Universities (Grant No. 2019ZD04), and the Fund of Guangdong Provincial Key Laboratory of Luminescence from Molecular Aggregates (Grant No. 2019B030301003).

Conflict of Interest

The authors declare no conflict of interest.

Keywords

dark state, enhanced emission, Herzberg–Teller effect, vibronic coupling

Received: March 11, 2020
Revised: April 17, 2020
Published online:

[1] C. W. Tang, S. A. VanSlyke, *Appl. Phys. Lett.* **1987**, *51*, 913.
[2] S. Reineke, F. Lindner, G. Schwartz, N. Seidler, K. Walzer, B. Lüssem, K. Leo, *Nature* **2009**, *459*, 234.
[3] J. Luo, Z. Xie, J. W. Y. Lam, L. Cheng, H. Chen, C. Qiu, H. S. Kwok, X. Zhan, Y. Liu, D. Zhu, B. Z. Tang, *Chem. Commun.* **2001**, 1740.
[4] J. Yang, Z. G. Chi, W. H. Zhu, B. Z. Tang, Z. Li, *Sci. China: Chem.* **2019**, *62*, 1900.
[5] Y. H. Wu, K. Huang, S. F. Chen, Y. Z. Chen, C.-H. Tung, L. Z. Wu, *Sci. China: Chem.* **2019**, *62*, 1194.
[6] B. Z. Tang, X. Zhan, G. Yu, P. P. Sze Lee, Y. Liu, D. Zhu, *J. Mater. Chem.* **2001**, *11*, 2974.
[7] M. Shimizu, H. Tatsumi, K. Mochida, K. Shimono, T. Hiyama, *Chem. - Asian J.* **2009**, *4*, 1289.
[8] P. Galer, R. C. Korošec, M. Vidmar, B. Šket, *J. Am. Chem. Soc.* **2014**, *136*, 7383.
[9] Q. Li, Z. Li, *Adv. Sci.* **2017**, *4*, 1600484.
[10] Q. Li, Z. Li, *Sci. China Mater.* **2020**, *63*, 177.
[11] N. L. C. Leung, N. Xie, W. Yuan, Y. Liu, Q. Wu, Q. Peng, Q. Miao, J. W. Y. Lam, B. Z. Tang, *Chem. - Eur. J.* **2014**, *20*, 15349.
[12] J. He, B. Xu, F. Chen, H. Xia, K. Li, L. Ye, W. Tian, *J. Phys. Chem. C* **2009**, *113*, 9892.
[13] Z. Yu, Y. Duan, L. Cheng, Z. Han, Z. Zheng, H. Zhou, J. Wu, Y. Tian, *J. Mater. Chem.* **2012**, *22*, 16927.
[14] H. J. Tracy, J. L. Mullin, W. T. Klooster, J. A. Martin, J. Haug, S. Wallace, I. Rudloe, K. Watts, *Inorg. Chem.* **2005**, *44*, 2003.
[15] K. A. N. Upamali, L. A. Estrada, P. K. De, X. Cai, J. A. Krause, D. C. Neckers, *Langmuir* **2011**, *27*, 1573.

[16] H. Zhou, J. Li, M. H. Chua, H. Yan, Q. Ye, J. Song, T. T. Lin, B. Z. Tang, J. Xu, *Chem. Commun.* **2016**, *52*, 12478.
[17] H. Zhou, Q. Ye, X. Wu, J. Song, C. M. Cho, Y. Zong, B. Z. Tang, T. S. A. Hor, E. K. L. Yeow, J. Xu, *J. Mater. Chem. C* **2015**, *3*, 11874.
[18] B. Z. Tang, *Sci. China: Chem.* **2018**, *61*, 377.
[19] M. Shimizu, Y. Asai, Y. Takeda, A. Yamatani, T. Hiyama, *Tetrahedron Lett.* **2011**, *52*, 2633.
[20] J. Mei, N. L. C. Leung, R. T. K. Kwok, J. W. Y. Lam, B. Z. Tang, *Chem. Rev.* **2015**, *115*, 11718.
[21] J. Mei, Y. Hong, J. W. Y. Lam, A. Qin, Y. Tang, B. Z. Tang, *Adv. Mater.* **2014**, *26*, 5429.
[22] H. Zhou, M. H. Chua, B. Z. Tang, J. Xu, *Polym. Chem.* **2019**, *10*, 3822.
[23] H. Zhou, X. Wang, T. T. Lin, J. Song, B. Z. Tang, J. Xu, *Polym. Chem.* **2016**, *7*, 6309.
[24] H. Zhou, J. Li, M. H. Chua, H. Yan, B. Z. Tang, J. Xu, *Polym. Chem.* **2014**, *5*, 5628.
[25] D. Oelkrug, A. Tompert, J. Gierschner, H.-J. Egelhaaf, M. Hanack, M. Hohloch, E. Steinhuber, *J. Phys. Chem. B* **1998**, *102*, 1902.
[26] Q. Peng, Y. P. Yi, Z. G. Shuai, J. S. Shao, *J. Am. Chem. Soc.* **2007**, *129*, 9333.
[27] Q. Wu, T. Zhang, Q. Peng, D. Wang, Z. Shuai, *Phys. Chem. Chem. Phys.* **2014**, *16*, 5545.
[28] T. Zhang, Q. Peng, C. Quan, H. Nie, Y. Niu, Y. Xie, Z. Zhao, B. Z. Tang, Z. Shuai, *Chem. Sci.* **2016**, *7*, 5573.
[29] X. Zheng, Q. Peng, L. Zhu, Y. Xie, X. Huang, Z. Shuai, *Nanoscale* **2016**, *8*, 15173.
[30] Q. Li, L. Blancafort, *Chem. Commun.* **2013**, *49*, 5966.
[31] X.-L. Peng, S. Ruiz-Barragan, Z.-S. Li, Q.-S. Li, L. Blancafort, *J. Mater. Chem. C* **2016**, *4*, 2802.
[32] Y. Tu, J. Liu, H. Zhang, Q. Peng, J. W. Y. Lam, B. Z. Tang, *Angew. Chem.* **2019**, *58*, 14911.
[33] J. W. Chung, S.-J. Yoon, B.-K. An, S. Y. Park, *J. Phys. Chem. C* **2013**, *117*, 11285.
[34] T. Mutai, H. Sawatani, T. Shida, H. Shono, K. Araki, *J. Org. Chem.* **2013**, *78*, 2482.
[35] J. V. Morris, U. Brühlmann, O. Serafimov, J. R. Huber, *Phys. Chem.* **1974**, *78*, 1348.
[36] H. M. McConnell, *J. Chem. Phys.* **1961**, *35*, 508.
[37] J. Goodman, L. E. Brus, *J. Chem. Phys.* **1978**, *69*, 1604.
[38] J. Li, C.-K. Lin, X. Y. Li, C. Y. Zhu, S. H. Lin, *Phys. Chem. Chem. Phys.* **2010**, *12*, 14967.
[39] G. Herzberg, E. Teller, *Z. Phys. Chem.* **1933**, *21B*, 410.
[40] F. Santoro, A. Lami, R. Improta, J. Bloino, V. Barone, *J. Chem. Phys.* **2008**, *128*, 224311.
[41] F. Santoro, C. Cappelli, V. Barone, *J. Chem. Theory Comput.* **2011**, *7*, 1824.
[42] Z. Gasyna, P. N. Schatz, J. P. Hare, T. J. Dennis, H. W. Kroto, R. Taylor, D. R. M. Walton, *Chem. Phys. Lett.* **1991**, *183*, 283.
[43] P. Yang, D. Qi, G. You, W. Shen, M. Li, R. He, *J. Chem. Phys.* **2014**, *141*, 124304.
[44] Y.-H. Wang, M. Halik, C.-K. Wang, S. R. Marder, Y. Luo, *J. Chem. Phys.* **2005**, *123*, 194311.
[45] A. C. Albrecht, *J. Chem. Phys.* **1960**, *33*, 169.
[46] S. Leach, M. Vervloet, A. Desprès, E. Bréheret, J. P. Hare, J. Dennis, T. H. W. Kroto, R. Taylor, D. R. M. Walton, *Chem. Phys.* **1992**, *160*, 451.
[47] M. Wykes, R. Parambil, D. Beljonne, J. Gierschner, *J. Chem. Phys.* **2015**, *143*, 114116.
[48] Y. Iwasa, T. Koda, S. Koshihara, Y. Tokura, N. Iwasawa, G. Saito, *Phys. Rev. B* **1989**, *39*, 10441.
[49] J. Lee, K. Shizu, H. Tanaka, H. Nakanotani, T. Yasuda, H. Kaji, C. Adachi, *J. Mater. Chem. C* **2015**, *3*, 2175.
[50] Z. G. Shuai, Q. Peng, *Natl. Sci. Rev.* **2017**, *4*, 224.
[51] Y. Niu, Q. Peng, C. Deng, X. Gao, Z. Shuai, *J. Phys. Chem. A* **2010**, *114*, 7817.
[52] Y. Niu, W. Li, Q. Peng, H. Geng, Y. Yi, L. Wang, G. Nan, D. Wang, Z. Shuai, *Mol. Phys.* **2018**, *116*, 1078.
[53] Y. Niu, Q. Peng, Z. Shuai, *Sci. China, Ser. B: Chem.* **2008**, *51*, 1153.
[54] D. Shukla, P. Wan, *J. Am. Chem. Soc.* **1993**, *115*, 2990.
[55] S. H. Lin, T.-S. Yang, M. Hayashi, F. C. Hsu, *Adv. Chem. Phys.* **2002**, *121*, 1.

